UNIVERSITY OF
Southampton
Institute of Sound and
Vibration Research

ISVR Technical Report

Theoretical Investigation of Phase Velocity, Group Velocity and Attenuation of Acoustic Waves in a Liquid-Filled Cylinder

K. Baik, J. Jiang and T.G. Leighton

ISVR Technical Report No 329

November 2009

SCIENTIFIC PUBLICATIONS BY THE ISVR

Technical Reports are published to promote timely dissemination of research results by ISVR personnel. This medium permits more detailed presentation than is usually acceptable for scientific journals. Responsibility for both the content and any opinions expressed rests entirely with the author(s).

Technical Memoranda are produced to enable the early or preliminary release of information by ISVR personnel where such release is deemed to the appropriate. Information contained in these memoranda may be incomplete, or form part of a continuing programme; this should be borne in mind when using or quoting from these documents.

Contract Reports are produced to record the results of scientific work carried out for sponsors, under contract. The ISVR treats these reports as confidential to sponsors and does not make them available for general circulation. Individual sponsors may, however, authorize subsequent release of the material.

UNIVERSITY OF SOUTHAMPTON

INSTITUTE OF SOUND AND VIBRATION RESEARCH

FLUID DYNAMICS AND ACOUSTICS GROUP

Theoretical Investigation of Phase Velocity, Group Velocity and Attenuation of Acoustic Waves in a Liquid-Filled Cylinder

by

K Baik, J Jiang and T G Leighton

ISVR Technical Report No. 329

November 2009

Authorized for issue by
Professor R J Astley

ACKNOWLEDGEMENTS

This work is supported by the Oak Ridge National Laboratory (ORNL), Tennessee, US. ORNL is managed by UT-Battelle, LLC, under contract DE-AC05-00OR22725 for the US Department of Energy. This work is also funded by the UK Science and Technology Research Council (Principle Investigator: T. G. Leighton). This formulation was developed to assist in understanding acoustic propagation in mercury-filled steel pipes at ORNL, in relate to neutron generation through Spallation Neutron Sources. The authors thank Bernie Riemer and Mark Wendel of ORNL for access to the facilities and helpful discussion of the problem and to Chris Densham, Ottone Caretta, and Tristan Davenne at the UK Science and Technology Research Council for advice and discussions. The authors are particularly grateful to Ron Roy of Boston University for helpful discussion on the problem.

CONTENTS

FIGURE CAPTIONS

ABSTRACT

Theoretical investigations are undertaken with the propagation of sound inside the tube filled with liquid. Previous theoretical works by Del Grosso's, Lafleur and Shields, and Elvira-Segura are here reviewed and extended to the complex domain in order to predict the attenuation, as well as the sound speed, of the modes as a function of frequency. Phase velocity, group velocity, the attenuation, and cut-off frequencies of modes are obtained for the water-filled PMMA (Perspex) tube of internal radius, b=4.445 cm, and thickness, h=0.5 cm in the range of the wavenumber-radius product, $k_1 b$, up to 18. The theory was then applied to the case of a stainless-steel pipe filled with mercury having the dimensions as used in the Spallation Neutron Source at Oak Ridge National Laboratory, Tennessee.

1 Introduction

The object of this investigation is to provide theoretical basis to measure bubble populations inside a pipe in the Spallation Neutron Source (SNS) at the Oak Ridge National Laboratory (ORNL). With respect to this, the phenomena of wave propagation inside a liquid-filled cylindrical tube encompasses the important mechanism of sound coupling between the fluid and the elastic pipe material. It is important that this phenomenon be understood, since many of the methods for inverting acoustical observables to determine the bubble population rely on interpreting the difference between the observable in the bubbly fluid, and its value in bubble-free conditions (Leighton, 2004). Critically, the 'bubble-free' value is almost always taken to refer to the value of the bulk liquid. However when the liquid is contained within a thin-wall pipe, the bubble-free value does not equal the value of the observable in an infinite body of liquid (Jacobi, 1948; Lin *et al*, 1956), and it is important that this difference is not interpreted in the inversion as being due to bubbles. The issue of coupling between the wall and the liquid affects the phase and group velocities and attenuation of the modes inside the tube. The theoretical formulations for these by Del Grosso (1971) and Lafleur and Shields (1985) have since been use in around two dozen later works (see for example Mert *et al.*, 2004; Wilson, 2002; Wilson *et al*, 2003, 2007).

Therefore in this report, propagation of the wave in water filled pipe is examined using theory to see how the coupling between the water and the tube wall changes the speed of sound and attenuation coefficient. The theoretical and experimental works done by Del Grosso (1971), Lafleur and Shields (1985), and Elvira-Segura (2000) are examined and re-derived in Sections 2 and 3 (the re-derivation is important to gain understanding, and also revealed errors in the original publications). Section 4 explains how the complex solutions were obtained using the extended formulations referred in the previous sections and through consideration of the material properties and absorption. This section also highlights the numerical methods to find the phase speed and the attenuation of the modes in wavenumber space. The numerical prediction of the dispersion relation in the current PMMA pipe is also shown in Section 5. Through the theoretical investigation, it is possible to anticipate the results in the real mercury-based system and these are also shown in Section 5.

2 Characteristic equation to axisymmetric modes inside the elastic tube filled with viscous liquid

The early work by Del Grosso (971) provided the theoretical axisymmetric modal dispersion relation in an infinite liquid-filled cylindrical tube, which was proven experimentally by Lafleur and Shields (1985). Their results specifically calculated the dispersion relation of axisymmetric propagation mode in a water-filled elastic tube. Del Grosso denoted those axisymmetric modes as ET*m* where 'E' refers to elastic wall and 'T' refers to finite thickness, such that each axisymmetric mode is identified by only one integer *m* which indicates radial modes. The gauge transformation decouples the motion of the modes as purely longitudinal and shear. This can be expressed as $\vec{S} = \nabla\phi + \nabla\times\vec{\psi}$ where $\vec{S}$ is a displacement vector, ϕ, the scalar potential, and $\vec{\psi}$, the vector potential. When the viscosity of the liquid is considered, displacement vector can be also expressed as the sum of these two potentials, and from the linearized Navier-Stokes equation, Elvira-Segura (2000) showed the resulting displacement vector in the liquid as follows:

$$\vec{S}^{L} = -\left\{\left[\frac{X_{0m}}{b}J_1\left(\frac{rX_{0m}}{b}\right)\right]E + \left[iq_{0m}J_1(\varepsilon r)\right]F\right\}\hat{r} + \left\{\left[iq_{0m}J_0\left(\frac{rX_{0m}}{b}\right)\right]E + \left[\varepsilon J_0(\varepsilon r)\right]F\right\}\hat{z} \quad (2.1)$$

where

$$\varepsilon^2 = \frac{i\rho_L\omega}{\eta} - q_{0m}^2, \qquad \left(\frac{X_{0m}}{b}\right)^2 = k_1'^2 - q_{0m}^2,\ k_1'^2 = \left[\frac{1}{k_1^{\,2}} - \frac{i}{\rho_L\omega}\left(\frac{4}{3}\eta + \eta_B\right)\right]^{-1}.$$

In elastic solid, assuming the dependence of $\exp[i(q_{0m}z - \omega t)]$, scalar potential, ϕ, and the vector potential, $\vec{\psi}$ satisfy the Helmholtz equation in cylindrical coordinates as follows:

$$\frac{\partial^2 \phi}{\partial r^2} + \frac{1}{r}\frac{\partial \phi}{\partial r} + P_m^2 \phi = 0, \tag{2.2a}$$

$$\frac{\partial^2 \psi_r}{\partial r^2} + \frac{1}{r}\frac{\partial \psi_r}{\partial r} + \left(T_m^2 - \frac{1}{r^2}\right)\psi_r = 0, \tag{2.2b}$$

$$\frac{\partial^2 \psi_\theta}{\partial r^2} + \frac{1}{r}\frac{\partial \psi_\theta}{\partial r} + \left(T_m^2 - \frac{1}{r^2}\right)\psi_\theta = 0, \tag{2.2c}$$

$$\frac{\partial^2 \psi_z}{\partial r^2} + \frac{1}{r}\frac{\partial \psi_z}{\partial r} + T_m^2 \psi_z = 0, \tag{2.2d}$$

where

$$P_m^2 = k_c^2 - q_{0m}^2,\ T_m^2 = k_s^2 - q_{0m}^2,$$

and $k_c = \omega / C_c$, $k_s = \omega / C_s$, and $k_1 = \omega / C_1$. The terms C_c and C_s represent the longitudinal speed and shear speed of the tube material respectively and C_1 is the intrinsic speed of sound in the liquid.

The solution of the above equation is the well known Bessel function. The solutions of Eqs. (2.2a) and (2.2d} are zeroth order Bessel functions and the solutions of Eqs. (2.2b) and (2.2c) are first order Bessel functions. Each Bessel function can be expressed either in terms of $J_n(x)$, $Y_n(x)$, and Hankel functions. Thus, the displacement vector in elastic solid in axisymmetric case becomes:

$$\begin{aligned}\vec{S}^E = &-\{P_m[AJ_1(rP_m) + BY_1(rP_m)] + iq_{0m}[CJ_1(rT_m) + DY_1(rT_m)]\}\hat{r} \\ &+ \{iq_{0m}[AJ_0(rP_m) + BY_0(rP_m)] + T_m[CJ_0(rT_m) + DY_0(rT_m)]\}\hat{z}.\end{aligned} \tag{2.3}$$

Thus, radial displacement is composed of first order Bessel functions and the axial displacement consists of zeroth order Bessel functions. In cylindrical coordinates, the stress components are described in terms of displacement as:

$$\tau_{rr} = \lambda\left(\frac{\partial S_r}{\partial r} + \frac{S_r}{r} + \frac{1}{r}\frac{\partial S_\theta}{\partial \theta} + \frac{\partial S_z}{\partial z}\right) + 2\mu\frac{\partial S_r}{\partial r}, \tag{2.4a}$$

$$\tau_{r\theta} = \mu\left(\frac{1}{r}\frac{\partial S_r}{\partial \theta} + \frac{\partial S_\theta}{\partial r} - \frac{S_\theta}{r}\right), \tag{2.4b}$$

$$\tau_{rz} = \mu\left(\frac{\partial S_r}{\partial z} + \frac{\partial S_z}{\partial r}\right), \tag{2.4c}$$

where μ and λ are Lamé constants. In the axisymmetric cylindrical coordinates, all the terms derived with respect to angle θ vanishes. Figure 2.1 shows the liquid-filled elastic tube with inner and outer radii *b* and *d* respectively.

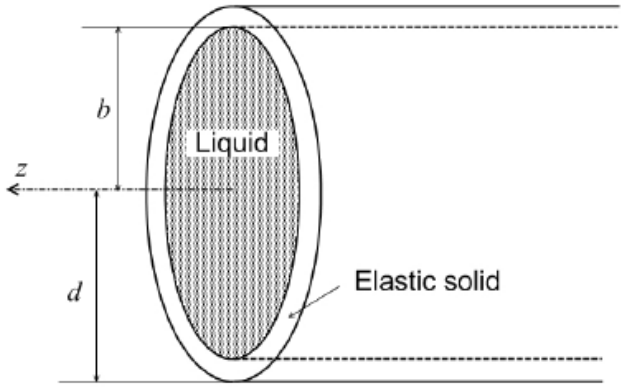

Figure 2.1 Geometry of infinite liquid cylinder. Inner and outer radii are *b* and *d* respectively.

In this geometry, the resulting pressure in the liquid and the element of the stress tensor in the tube wall calculated from Eq. (2.4) becomes:

$$p = -\left[\rho_L C_1^2 k_1'^2 J_0\left(\frac{rX_{0m}}{b}\right)\right]E, \tag{2.5a}$$

$$\begin{aligned}\tau_{rr}^E = &-\lambda\left(P_m^2 + q_{0m}^2\right)\left[AJ_0(rP_m) + BY_0(rP_m)\right] \\ &- 2\mu\left\{P_m^2\left[AJ_0(rP_m) + BY_0(rP_m)\right] + iT_m q_{0m}\left[CJ_0(rT_m) + BY_1(rT_m)\right]\right\} \\ &+ 2\mu\left\{\frac{P_m}{r}\left[AJ_1(rP_m) + BY_1(rP_m)\right] + i\frac{q_{0m}}{r}\left[CJ_1(rT_m) + DY_1(rT_m)\right]\right\},\end{aligned} \tag{2.5b}$$

$$\tau_{rz}^E = \mu\left\{-2iP_m q_{0m}\left[AJ_1(rP_m) + BY_1(rP_m)\right] + \left(q_{0m}^2 - T_m^2\right)\left[CJ_1(rT_m) + DY_1(rT_m)\right]\right\}, \tag{2.5c}$$

where the superscripts '*L*' and '*E*' denote the terms relate to the liquid and the elastic tube respectively. The density of the tube, ρ_E, Lamé constants, shear speed, C_s, and Poisson's ratio ν are related with each other as follows:

$$\lambda = \frac{2\nu}{1-2\nu}\rho_E C_s^2, \ \mu = \rho_E C_s^2. \tag{2.6}$$

In the expression of Eqs. (2.1), (2.3), and (2.5), the factor $\exp\left[i\left(q_{0m}z-\omega t\right)\right]$ is common to each term and it was omitted to simplify the notation

In Eqs. (2.1), (2.3), and (2.5), *A*, *B*, *C*, *D*, *E*, and *F* are constants determined from the six boundary conditions, that are described as the continuity of the normal displacement, the normal stress, and the shear stress tensor at both *r=b* and *r=d* in Fig. 2.1. Shear displacement was not considered in the lossless case. However, in the case of considering viscosity, a *no slip* condition is included and this requires continuity of the shear displacement and the shear stress at the liquid-tube interface. The continuity of the shear stress tensor at both *r=b* and *r=d* reveals that:

$$A\left[iP_m q_{0m} J_1\left(bP_m\right)\right] + B\left[iP_m q_{0m} Y_1\left(bP_m\right)\right] + C\left[-E_m J_1\left(bT_m\right)\right] + D\left[-E_m Y_1\left(bT_m\right)\right] = 0, \tag{2.7a}$$

$$A\left[iP_m q_{0m} J_1\left(dP_m\right)\right] + B\left[iP_m q_{0m} Y_1\left(dP_m\right)\right] + C\left[-E_m J_1\left(dT_m\right)\right] + D\left[-E_m Y_1\left(dT_m\right)\right] = 0, \tag{2.7b}$$

where

$$E_m = q_{0m}^2 - \frac{k_s^2}{2}.$$

Continuity of the normal stress tensor gives:

$$\left[E_m J_0(bP_m)+\frac{P_m}{b}J_1(bP_m)\right]A+\left[E_m Y_0(bP_m)+\frac{P_m}{b}Y_1(bP_m)\right]B$$
$$+\left[-iq_{0m}T_m J_0(bT_m)+\frac{iq_{0m}}{b}J_1(bT_m)\right]C+\left[-iq_{0m}T_m Y_0(bT_m)+\frac{iq_{0m}}{b}Y_1(bT_m)\right]D \quad (2.8a)$$
$$=-\left[\frac{\rho_L C_1^2 k_1'^2}{2\rho_E C_s^2}J_1(X_{0m})\right]E,$$

$$\left[E_m J_0(dP_m)+\frac{P_m}{d}J_1(dP_m)\right]A+\left[E_m Y_0(dP_m)+\frac{P_m}{d}Y_1(dP_m)\right]B$$
$$+\left[-iq_{0m}T_m J_0(dT_m)+\frac{iq_{0m}}{d}J_1(dT_m)\right]C+\left[-iq_{0m}T_m Y_0(dT_m)+\frac{iq_{0m}}{b}Y_1(dT_m)\right]D \quad (2.8b)$$
$$=0,$$

Continuity of the normal and the shear displacement at the liquid-tube interface gives:

$$[P_m J_1(bP_m)]A+[P_m Y_1(bP_m)]B+[iq_{0m}J_1(bT_m)]C+[iq_{0m}Y_1(bT_m)]D$$
$$=\left[\frac{X_{0m}}{b}J_1(X_{0m})\right]E+[iq_{0m}J_1(\varepsilon b)]F, \quad (2.9a)$$

$$[iq_{0m}J_0(bP_m)]A+[iq_{0m}Y_0(bP_m)]B+[T_m J_0(bT_m)]C+[T_m Y_0(bT_m)]D$$
$$=[iq_{0m}J_0(X_{0m})]E+[\varepsilon J_1(\varepsilon b)]F. \quad (2.9b)$$

Each term associated with the coefficient *F* in Eqs. (2.9a) and (2.9b) reveals typographical errors in Eqs. (12c) and (12d) respectively of Elvira-Segura's paper (Elvira-Segura, 2000). All the terms associated with the coefficient *F* in his paper were normalized by the wavenumber, *a* (equivalent to ε in our study), which makes the dimensions of those terms ([1/ m^2]) different from the dimensions of the terms ([1/m]) associated with other coefficients, where [m] represents the dimension of length. However, this error does not affect the resulting characteristic equation (although he did not obtain an analytic expression for the characteristic equation like Eq. (2.11) in this report) for the following reason. Jumping to Eq. (2.11) and investigating the Bessel functions, $\varepsilon J_0(\varepsilon b)$ and $J_1(\varepsilon b)$, it is clear that those are always coupled with the denominator K_m defined in Eq. (2.10b). Thus, they appear in the equation in the form of $\varepsilon J_0(\varepsilon b)/K_m$ and $J_1(\varepsilon b)/K_m$. Dividing both numerators and denominators of those by ε does not affect the characteristic resulting equation, and this

means, using $J_0(\varepsilon b)$ and $J_1(\varepsilon b)/\varepsilon$ instead of $\varepsilon J_0(\varepsilon b)$ and $J_1(\varepsilon b)$ does not affect the characteristic equation.

Although non-trivial solutions to Eqs. (2.7)-(2.9) are given by the determinant of a 6×6 matrix, this can be reduced to the determinant of a 4×4 matrix by eliminating coefficients *E* and *F* from Eqs. (2.8a) and (2.9a)-(2.9b) which can be described as one equation with only four coefficients *A*, *B*, *C*, and *D*, as follows:

$$\left[E_m J_0(bP_m)+P_m\frac{1+bQ_A}{b}J_1(bP_m)\right]A+\left[E_m Y_0(bP_m)+P_m\frac{1+bQ_B}{b}Y_1(bP_m)\right]B$$
$$+iq_{0m}\left[-T_m J_0(bT_m)+\frac{1+bQ_C}{b}J_1(bT_m)\right]C+iq_{0m}\left[-T_m Y_0(bT_m)+\frac{1+bQ_D}{b}Y_1(bT_m)\right]D \quad (2.10a)$$
$$=0,$$

where

$$Q_A=\frac{\varepsilon J_0(\varepsilon b)+\left(q_{0m}^2/P_m\right)\left[J_0(bP_m)/J_1(bP_m)\right]J_1(\varepsilon b)}{K_m}Q'_{m,}$$

$$Q_B=\frac{\varepsilon J_0(\varepsilon b)+\left(q_{0m}^2/P_m\right)\left[Y_0(bP_m)/Y_1(bP_m)\right]J_1(\varepsilon b)}{K_m}Q'_{m,}$$

$$Q_C=\frac{\varepsilon J_0(\varepsilon b)-T_m\left[J_0(bT_m)/J_1(bT_m)\right]J_1(\varepsilon b)}{K_m}Q'_{m,}$$

$$Q_D=\frac{\varepsilon J_0(\varepsilon b)-T_m\left[Y_0(bT_m)/Y_1(bT_m)\right]J_1(\varepsilon b)}{K_m}Q'_{m,}$$

$$K_m=\varepsilon J_0(\varepsilon b)+\left(bq_{0m}^2/X_{0m}\right)\left[J_0(X_{0m})/J_1(X_{0m})\right]J_1(\varepsilon b),$$

$$Q'_m=\frac{\rho_L k_1'^2 C_1^2 b J_0(X_{0m})}{2\rho_E C_s^2 X_{0m} J_1(X_{0m})}. \quad (2.10b)$$

In the inviscid case where $\varepsilon\to\infty$, all the quantities, Q_A, Q_B, Q_C, and Q_D approach Q_m as explained in the next section and Eq. (2.10a) becomes identical to Eq. (4d) in the paper by Lafleur and Shields (1985), except that the latter has two typographical errors. Comparing Eq. (2.10a) in the inviscid limit with Eq. (4d) of Lafleur and Shields (1985), P_m should be added at the second term of the second line and *d* should be substituted as *b* at the second

term of the fourth line in Eq. (4d) of their paper. However, their typographical errors in Eq. (4d) do not affect the resulting characteristic Eq. (5) in their paper because it was calculated based upon the corrected expression for Eq. (4d).

The characteristic equation which describes the propagation of the wave inside the cylindrical tube filled with viscous liquid is obtained by expanding the determinant of a 4×4 matrix determined by Eqs. (2.7a), (2.7b), (2.8b), and (2.10a) and the result is as follows:

$$
\begin{aligned}
&1+\frac{J_1(\varepsilon b)}{2K_m}\left(\frac{q_{0m}^2}{E_m}+1\right)Q_m' \\
&+\left(1+\frac{J_1(\varepsilon b)}{K_m}Q_m'\right)\left[L_{00}(T_m)L_{11}(P_m)\right]\frac{\pi^2 T_m^2 P_m^2 q_{0m}^2 bd}{8E_m^2} \\
&+\left(1+\frac{q_{0m}^2 J_1(\varepsilon b)}{E_m K_m}Q_m'\right)\left[L_{11}(T_m)L_{00}(P_m)\right]\frac{\pi^2 E_m^2 bd}{8q_{0m}^2} \\
&+\left[\left(1+\frac{q_{0m}^2 J_1(\varepsilon b)}{E_m K_m}Q_m'\right)L_{01}(T_m)L_{10}(P_m)+\left(1+\frac{J_1(\varepsilon b)}{K_m}Q_m'\right)L_{10}(T_m)L_{01}(P_m)\right]\frac{\pi^2 T_m P_m bd}{8} \\
&+\left[b\left(1+\frac{J_1(\varepsilon b)}{K_m}Q_m'\right)L_{10}(T_m)L_{11}(P_m)+d\left(1+\frac{\varepsilon b J_0(\varepsilon b)}{K_m}Q_m'\right)L_{01}(T_m)L_{11}(P_m)\right] \\
&\times\left(\frac{\pi^2 T_m P_m^2}{8E_m}-\frac{\pi^2 T_m P_m^2 q_{0m}^2}{8E_m^2}\right) \\
&+\left[b\left(1+\frac{q_{0m}^2 J_1(\varepsilon b)}{E_m K_m}Q_m'\right)L_{11}(T_m)L_{10}(P_m)+d\left(1+\frac{\varepsilon b J_0(\varepsilon b)}{K_m}Q_m'\right)L_{11}(T_m)L_{01}(P_m)\right] \\
&\times\left(\frac{\pi^2 P_m E_m}{8q_{0m}^2}-\frac{\pi^2 P_m}{8}\right) \qquad (2.11) \\
&+\left(1+\frac{\varepsilon b J_0(\varepsilon b)}{K_m}Q_m'\right)L_{11}(T_m)L_{11}(P_m)\left(\frac{\pi^2 P_m^2}{8q_{0m}^2}+\frac{\pi^2 P_m^2 q_{0m}^2}{8E_m^2}-\frac{\pi^2 P_m^2}{4E_m}\right)=0,
\end{aligned}
$$

where, the Wronskian, L_{mn} is defined by $L_{mn}(y)=J_m(dy)Y_n(by)-J_n(by)Y_m(dy)$. Equation (2.11) is equivalent to the formulation by Elvira-Segura which is given by the determinant of 6×6 matrix.

3 Lossless solution to axisymmetric modes in a inviscid liquid-filled elastic tube

The lossless case in the liquid corresponds to the situation where the viscous effect in liquid vanishes. Consequently, when the shear and bulk viscosity coefficients, η and η_B, go to zero, ε diverges accordingly. In this limit, the quantity K_m defined in Eq. (2.10b) approaches $\varepsilon J_0(\varepsilon b)$ and following approximation hold in Eq. (2.11):

$$\lim_{\varepsilon\to\infty}\frac{J_1(\varepsilon b)}{K_m}=\lim_{\varepsilon\to\infty}\frac{J_1(\varepsilon b)}{\varepsilon J_0(\varepsilon b)}\to 0,\qquad \lim_{\varepsilon\to\infty}\frac{\varepsilon b J_0(\varepsilon b)}{K_m}=\lim_{\varepsilon\to\infty}\frac{\varepsilon b J_0(\varepsilon b)}{\varepsilon J_0(\varepsilon b)}\to b. \quad (3.1)$$

Thus, at this zero viscosity limit, k_1' defined in Eq. (2.1) converges to k_1 and all the quantities, Q_A, Q_B, Q_C, and Q_D defined in Eq. (2.10b) approach Q_m which is obtained by replacing k_1' with k_1 in the expression of Q_m'. Therefore, in the lossless case, Eq. (2.11) is reduced to the following formulations given by Del Grosso (1971) and Lafleur and Shields (1985).

$$\begin{aligned}
&1+\left[L_{00}(T_m)L_{11}(P_m)\right]\frac{\pi^2T_m^2P_m^2q_{0m}^2bd}{8E_m^2}+\left[L_{11}(T_m)L_{00}(P_m)\right]\frac{\pi^2E_m^2bd}{8q_{0m}^2}\\
&+\left[L_{01}(T_m)L_{10}(P_m)+L_{10}(T_m)L_{01}(P_m)\right]\frac{\pi^2T_mP_mbd}{8}\\
&+\left[bL_{10}(T_m)L_{11}(P_m)+d(1+bQ_m)L_{01}(T_m)L_{11}(P_m)\right]\left(\frac{\pi^2T_mP_m^2}{8E_m}-\frac{\pi^2T_mP_m^2q_{0m}^2}{8E_m^2}\right)\\
&+\left[bL_{11}(T_m)L_{10}(P_m)+d(1+bQ_m)L_{11}(T_m)L_{01}(P_m)\right]\left(\frac{\pi^2P_mE_m}{8q_{0m}^2}-\frac{\pi^2P_m}{8}\right)\\
&+(1+bQ_m)L_{11}(T_m)L_{11}(P_m)\left(\frac{\pi^2P_m^2}{8q_{0m}^2}+\frac{\pi^2P_m^2q_{0m}^2}{8E_m^2}-\frac{\pi^2P_m^2}{4E_m}\right)=0,
\end{aligned} \quad (3.2)$$

This characteristic equation cannot be solved analytically, but roots to q_{0m} can be found using numerical manipulation by appropriate mathematical software. Figures 3.1 and 3.2 show the normalized phase and group velocities of axisymmetric modes in the water-filled PMMA pipe as a function of frequency. The material properties in the calculations are shown

in Table 5.1 (Hartmann and Jarzynski, 1972; Hefner and Marston, 2000). The phase velocity of each mode is calculated as $C_{0m} = \omega / q_{0m}$ from roots to q_{0m}. At the zero frequency limit, two modes (the subsonic mode-ET0 and the supersonic mode-ET1) exist at $C_{00} / C_1 = 0.343$ and $C_{01} / C_1 = 1.552$. The phase velocities of other modes (ET2 and higher modes) become infinite at their cut-off frequency. As the frequency increases, the phase velocity of the ET1 mode converges to C_1, the speed of sound in water, and the phase velocity of the ET0 mode approaches $C_{00} / C_1 = 0.63$. Other higher modes can be seen, and their phase velocities decrease as the frequency increases.

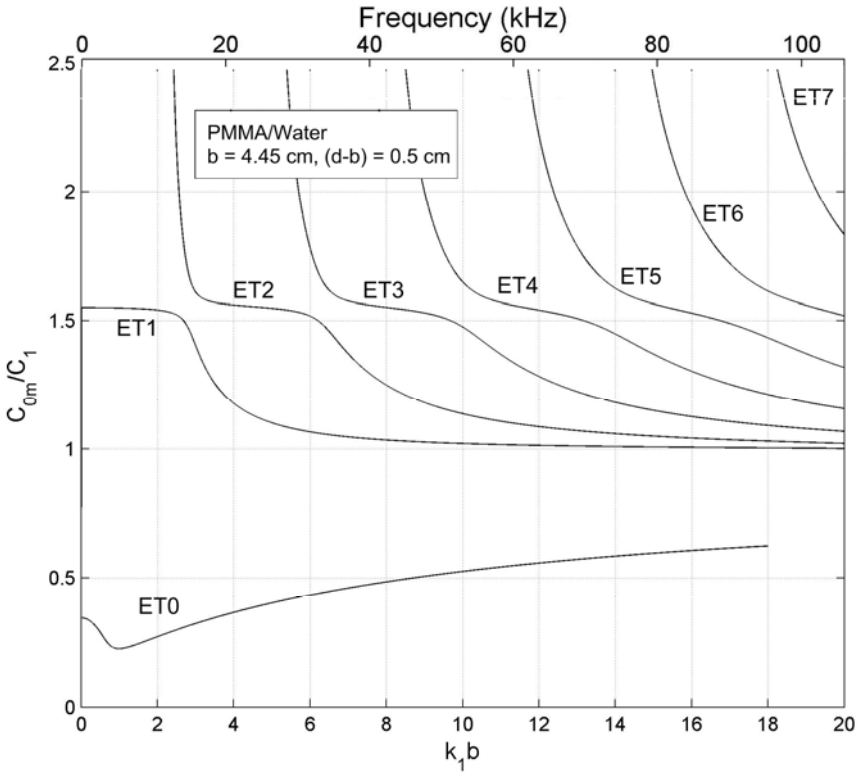

Figure 3.1: Normalized phase velocity of axisymmetric modes in the water-filled PMMA (Perspex) pipe as a function of frequency. The material properties of PMMA are shown in Table 5.1.

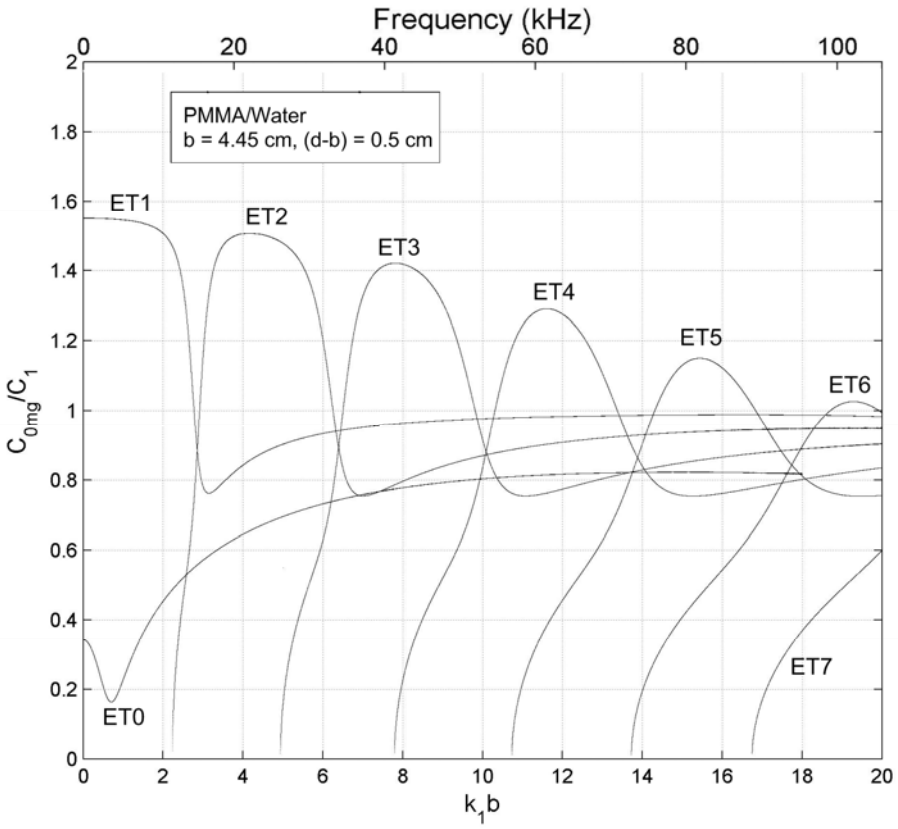

Figure 3.2: Normalised group velocity of axiymmetric modes in the water-filled PMMA pipe as a function of frequency.

Group velocities can be easily found from the calculated phase velocities using following relation where c_l is phase velocity and c_g is group velocity (Grigsby, 1961).

$$\frac{C_{0mg}}{C_1} = \frac{C_{0m}}{C_1}\left[1 - \frac{1}{1 - \dfrac{C_{0m}/C_1}{k_1 b \dfrac{d\left(C_{0m}/C_1\right)}{d\left(k_1 b\right)}}}\right]. \qquad (3.3)$$

Although ET2 and the higher modes have infinite phase velocities at the cut-off frequency limit, their group velocities approach zero at their cut-off frequencies. The consequence of this is that these modes do not exist at driving frequencies that are less than their cut-off frequencies. The cut-off frequency of the mode is obtained from Eq. (3.2) at the limit of

$q_{0m} \to 0$. Multiplying both sides of Eq. (3.2) by q_{0m}, then eliminating vanishing terms as q_{0m} goes to zero, and arranging remaining terms, allows Eq. (3.2) to be reduced as follows:

$$bdk_s^4 L_{00}(k_c) - 2k_c k_s^2 \left[bL_{10}(k_c) + d\left(1 + Q_m^c b\right) L_{01}(k_c) \right] + 4k_c^2 \left(1 + Q_m^c b\right) L_{11}(k_c) = 0, \quad (3.4)$$

where

$$Q_m^c = \frac{\rho_L k_s^2 J_0(k_1 b)}{2\rho_E k_1 J_1(k_1 b)}$$

is the limiting form of Q_m as $q_{0m} \to 0$. The cut-off frequencies of the modes are given by the roots of Eq. (3.4) when it is solved with respect to frequency ω. Table 3.1 shows the cut-off frequencies of the modes. The values of the frequencies are expressed in terms of dimensionless quantity $k_1 b$. Thus, below the cut-off frequencies, ET2 and higher modes do not exist and are not observed. Figure 3.3 shows the phase and group velocities of ET2 mode with the indication of its cut-off frequency. As the driving frequency approaches the cut-off frequency, the phase velocity goes to infinity and the group velocity goes to zero. Except for the ET0 and ET1 modes, all other modes have the same pattern as those shown in Figs. 3.3.

Table 3.1: Cut-off frequencies of the modes in water/PMMA pipes in dimensionless frequency $k_1 b$.

Mode	ET2	ET3	ET4	ET5	ET6	ET7
$k_1 b$	2.234	4.938	7.792	10.730	13.722	16.744

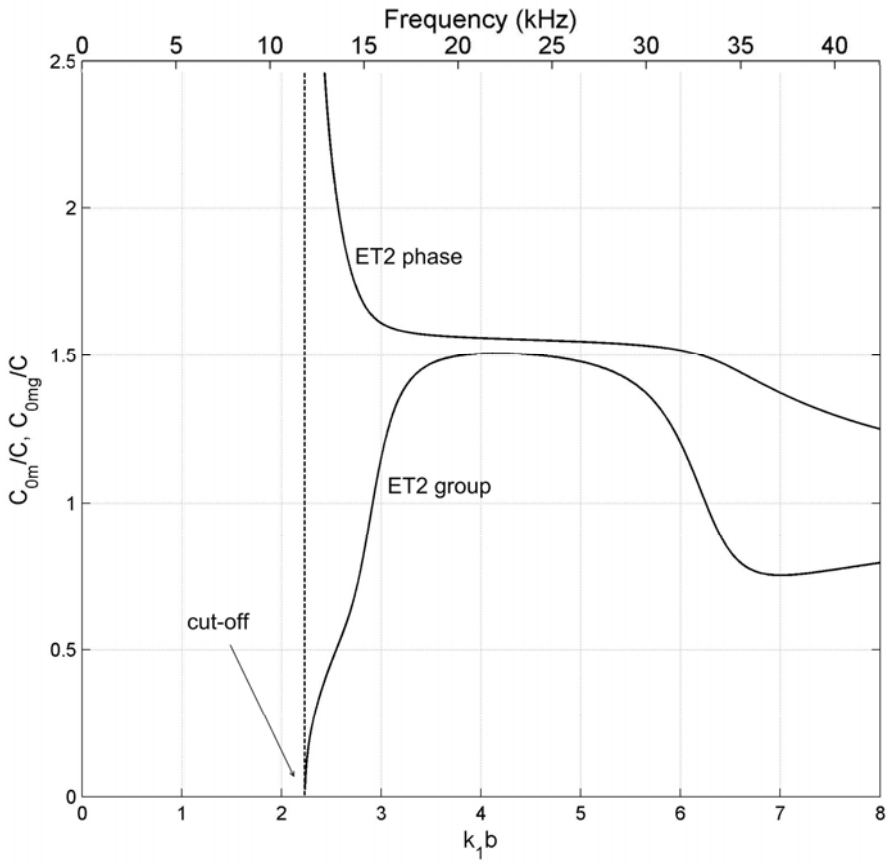

Figure 3.3: Phase and group velocities of ET2 mode. At the cut-off frequency, the phase velocity approaches infinity and the group velocity goes to zero.

It is helpful to understand the shape of each mode by investigating displacement profile of each mode. The displacement vector in the liquid is as shown in Eq. (2.1) with the constant E set equal to zero, which makes the terms associated with the viscosity vanish. The radial vector is described as the first order of Bessel function of the first kind and the axial vector is described as the zeroth order of Bessel function of the first kind. Normalization of the above with respect to the axial displacement at the center of the cylinder (r=0), generates the normalized displacement as follows:

$$\vec{S}_L^{norm} = \frac{iX_{0m}}{q_{0m}b} J_1\left(X_{0m}\frac{r}{b}\right)\hat{r} + J_0\left(X_{0m}\frac{r}{b}\right)\hat{z}, \tag{3.5}$$

Hence, for a given frequency, each mode has certain real value of q_{0m} and it is possible to depict the displacement profile as a function of radius r. Figures 3.4-3.7 show the normalized

displacements of ET0-ET3 modes at a certain frequency (as indicated on each picture). In each of these figures, panel (a) shows the magnitude of the normalized radial displacement and panel (b) shows the magnitude of the normalized axial displacement. From these figures, it is clear that the higher the order of the mode, the greater the number of local maxima or minima in the profile (as expected). One subsonic mode, ET0, shows higher magnitudes of displacements on the wall than any other location inside the liquid. This means the mode shape is more dependent on the acoustic coupling between the liquid and the elastic wall than is the shape of other modes. Therefore under conditions when the displacements on the liquid-wall interface are not sufficiently excited, this mode will not be observed. For the ET1 and the higher modes, the radial displacement and the axial displacement are always out of phase at the center ($r = 0$).

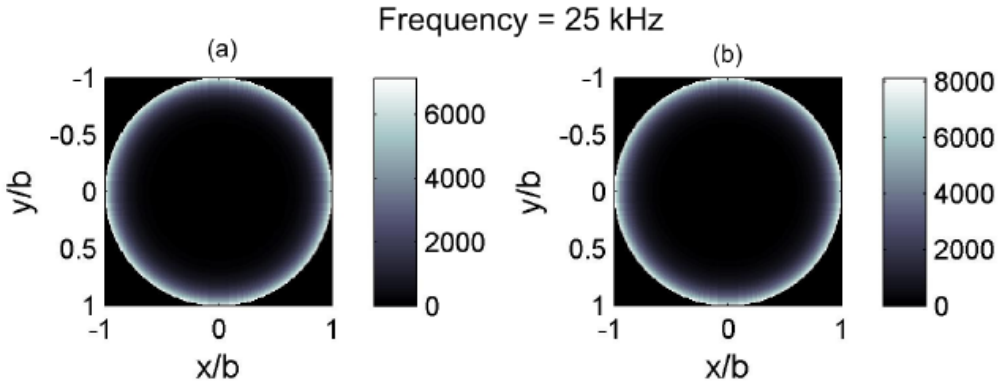

Figure 3.4: Magnitude of the (a) radial displacement and (b) axial displacement of ET0 mode. The magnitude of this mode increases dramatically at the interface of the tube wall ($r/b = \sqrt{x^2 + y^2}\,/b = 1$).

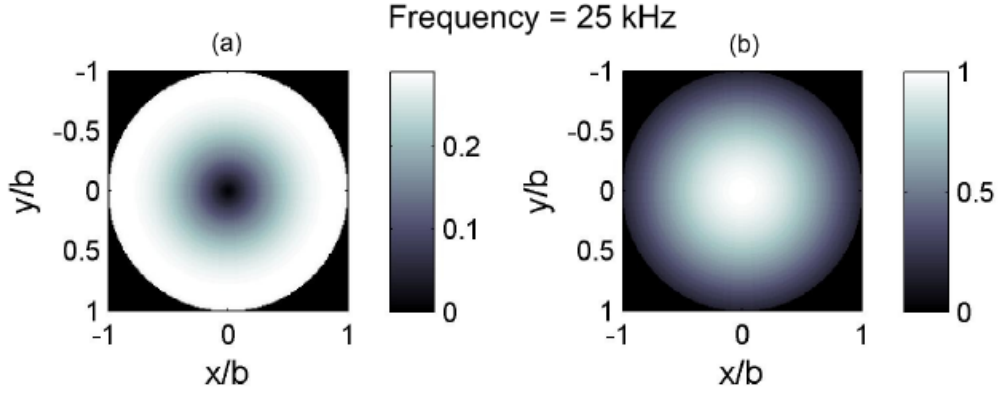

Figure 3.5: Magnitude of the (a) radial displacement and (b) axial displacement of ET1 mode.

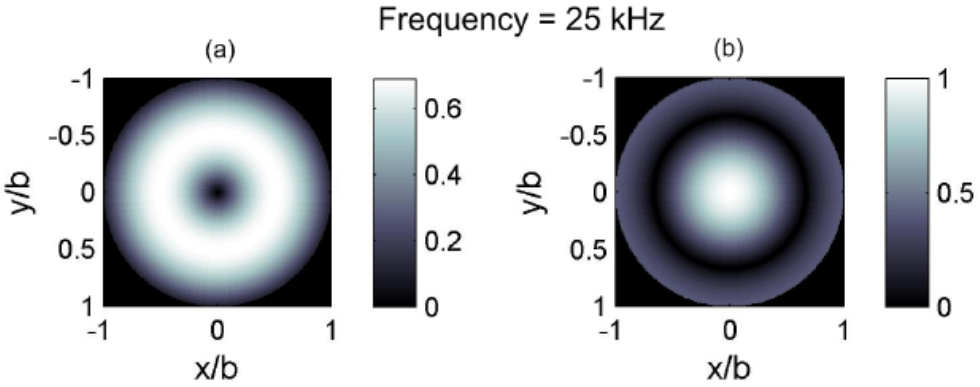

Figure 3.6: Magnitude of the (a) radial displacement and (b) axial displacement of ET2 mode.

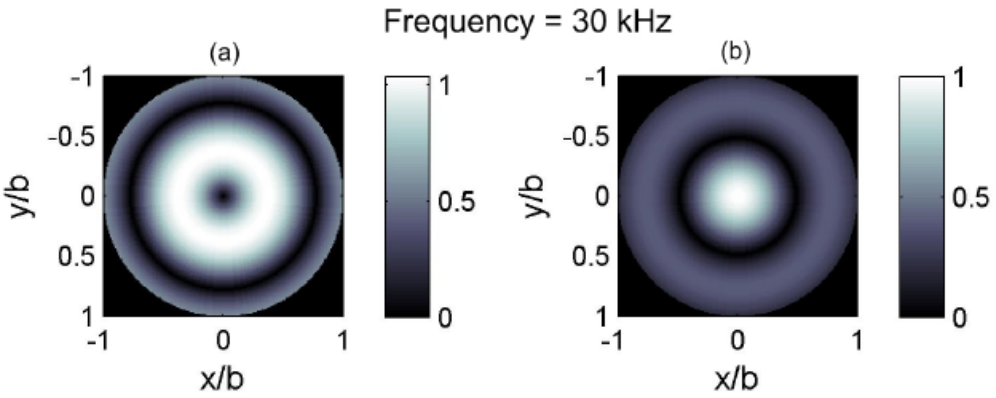

Figure 3.7: Magnitude of the (a) radial displacement and (b) axial displacement of ET3 mode.

At the zero frequency limit, the small argument approximation of Bessel function may be applied (Abramowitz *et al*, 1965):

$$J_n(z) \to \frac{1}{n!}\left(\frac{z}{2}\right)^n,$$

$$Y_n(z) \to \begin{cases} \dfrac{2}{\pi}\left[\ln\dfrac{z}{2} + \delta\right], & (n = 0) \\ -\dfrac{(n-1)!}{\pi}\left(\dfrac{2}{z}\right)^n, & (n > 0) \end{cases} \tag{3.6}$$

where δ = 0.57721… is Euler-Mascheroni constant. Therefore, at zero frequency limit, the values of $L_{mn}(z)$ (as defined in Eq. (3.2)) converge to:

$$L_{00}(z) \to \frac{2}{\pi}\ln\left(\frac{b}{d}\right), \tag{3.7a}$$

$$L_{01}(z) \to -\frac{2}{\pi bz} - \frac{bz}{\pi}\left[\ln\frac{dz}{2} + \delta\right], \tag{3.7b}$$

$$L_{10}(z) \to \frac{2}{\pi dz} + \frac{dz}{\pi}\left[\ln\frac{dz}{2} + \delta\right], \tag{3.7c}$$

$$L_{11}(z) \to \frac{1}{\pi}\left(\frac{b}{d} - \frac{d}{b}\right). \tag{3.7d}$$

At zero frequency limit where $\gamma \to 0$, the second terms in Eqs. (3.7b) and (3.7c) converge to zero. This can be easily shown by l'Hôpital's rule. Defining $y = d^2/b^2 - 1$ and substituting this into Eq. (3.7), following expression is obtained.

$$L_{00}(z) \to \frac{2}{\pi}\ln(y+1), \tag{3.8a}$$

$$L_{01}(z) \to -\frac{2}{\pi bz}, \tag{3.8b}$$

$$L_{10}(z) \to \frac{2}{\pi dz}, \tag{3.8c}$$

$$L_{11}(z) \to -\frac{y}{\pi\sqrt{y+1}}. \tag{3.8d}$$

Therefore, applying Eq. (3.8) to Eq. (3.2) and taking the leading terms as $\omega \to 0$, the following equation is obtained which describes the solution at zero frequency:

$$\begin{aligned}(3\beta - 4\alpha)yx^4 - \{4\gamma(\beta-\alpha) + [(3\beta-4\alpha)(1+\gamma) + \beta(\beta-\alpha)]y\}x^2 \\ + \beta^2\gamma + \beta(\beta-\alpha)(1+\gamma)y = 0\end{aligned}, \tag{3.9}$$

where

$$\alpha = \left(\frac{C_1}{C_c}\right)^2,\ \beta = \left(\frac{C_1}{C_s}\right)^2,\ \gamma = \beta\frac{\rho_L}{\rho_E},\ x = \frac{C_1}{C_{0m}},\ y = \frac{d^2}{b^2} - 1.$$

This is fourth order polynomial equation and easy to solve because it has perfect quadratic form. Substituting $X = x^2$, the above equation is reduced to a simple quadratic equation. Consequently the maximum number of real solutions for *X* is two (which we will term *a* and *b*). Because $X = x^2$, the solution *x* becomes $x = \pm a,\ \pm b$ if *a* and *b* are all positive. Because only positive solutions have meaning in the context of this study, the maximum number of real solutions to Eq. (3.9) is at most two (+*a* and +*b*). The above equation, Eq. (3.9), corresponds to Eq. (6) in the paper by Lafleur and Shields (1985) and their equation contains a typographical error. Comparing Eq. (3.9) above with Eq. (6) of Lafleur and Shields (1985), it is clear that ρ_W / ρ_L in the definition of the term γ should be inverted in Eq. (6) of Lafleur and Shields (1985). One can simply check this typographical error because the subsequent Figs. 3 and 4 in their paper match up to the zero frequency solution only when this typographical error is corrected in Eq. (6) in their paper (Their Figs. 3 and 4 show correct calculations at zero frequency limit, which cannot be obtained from Eq. (6) in their paper since it contains typographical error). Otherwise, the uncorrected Eq. (6) gives incorrect zero frequency solutions, which are distinctly observed for the ET0 mode of their Aluminum/Water case in reference Lafleur and Shields (1985). Although Eqs. (4d) and (6) of Lafleur and Shields contain typographical errors, their Eq. (5) does not (although readers should be aware that it has since been reproduced by later authors with typographical errors).

4 Complex solutions to the characteristic equation and technique of attenuation measurement

Complex solutions can be obtained by setting the material properties in both the elastic solid and the liquid inside as complex quantities. As stated in Section 2, the complex wavenumber in the liquid, k_1', is generated by the consideration of the viscosity of the liquid. Shear viscosity, η, and the bulk viscosity, η_B are related to the complex wavenumber, k_1', as

shown in Eq. (2.1). When the effects of liquid viscosity are small, the complex wavenumber k_1' can be approximated as:

$$k_1' \approx k_1 + i\frac{\omega^2}{2\rho_L C_1^3}\left(\frac{4}{3}\eta + \eta_B\right). \qquad (4.1)$$

The imaginary part of the complex wavenumber is equivalent to the expression for the classical absorption in liquid (Kinsler *et al*, 2000).

The material property in the elastic solid can be represented by expanding the real wavenumbers, k_s and k_c, in Eq. (2.11) to complex wavenumbers, k_s' and k_c' as follows:

$$k_s' = \frac{\omega}{C_s}(1 + i\gamma_s),\ k_c' = \frac{\omega}{C_c}(1 + i\gamma_c), \qquad (4.2)$$

where γ_s and γ_c are the dimensionless ultrasonic shear and longitudinal absorption coefficients respectively. For PMMA, those are measured as $\gamma_c = 0.0034$ and $\gamma_s = 0.0053$ by Hartmann and Jarzynski (Hartmann and Jarzynski, 1972; Hefner and Marston, 2000). The complex wavenumber in liquid, k_1', is already embedded in Eq. (2.11) from the consideration of the viscosity of the liquid which results in the viscous damping, usually the dominant mechanism for acoustic absorption. However, inclusion of the ultrasonic absorption by the elastic solid is necessary in the case when the absorption occurs through the acoustic coupling between the liquid and the tube wall. The effect of the absorption by the solid on the attenuation of the modes is expected to be large in most plastic tubes since their walls are less brittle than those of the metal tubes. Thus, substituting Eq, (4.2) into Eq. (2.11), at a given frequency, the solution to $q_{0m}' = \omega / C_{0m} + i\,\mathrm{Im}[q_{0m}']$ can be found in the complex domain and the imaginary part of the complex wavenumber, q_{0m}', is mainly accounted for the complex wavenumbers, k_s' and k_c' in the PMMA tube. The real part of the q_{0m}' gives the phase velocities of the modes and the normalized phase velocity of the mode can be calculated through $C_{0m} / C_1 = k_1 / \mathrm{Re}[q_{0m}']$. The imaginary part of the q_{0m}' gives the damping of the

corresponding modes, and the attenuation coefficients, in the unit of dB per unit length, can be calculated by $20\,\mathrm{Im}[q'_{0m}]\log_{10}(e)$.

Although the complex solutions can be found by substituting Eq. (4.2) into Eq. (2.11), nearly the same results can be also found from Eq. (3.2) (which is the characteristic equation for lossless solutions) by substituting Eqs. (4.1) and (4.2) into Eq. (3.2). The latter method is usually easier for obtaining similar numerical precision in the complex solutions. In most practical cases, the viscosity coefficients, η and η_B, are very small. This causes the complex wavenumber, ε, to be a complex quantity of which the imaginary part is much larger than the real component. Sometimes, such a situation makes the numerical implementation of the Bessel functions in complex space extremely difficult. Therefore, when the viscous effect is not large compared to the material absorption, Eq. (3.2) can be used instead of using Eq. (2.11) to obtain the complex solution by substituting k_s, k_c, and k_1 with k'_s, k'_c, and k'_1 into Eq. (3.2) where k'_1, k'_s, and k'_c are defined in Eqs. (4.1) and (4.2) respectively. The complex solution for the PMMA/water tube and the Steel/mercury tube are shown in the next section.

In the practical situation, measurements of the phase speed and the attenuation of the modes are not easy since, theoretically, infinite numbers of modes are mixed together and they propagate with different speeds. Unless the tube is sufficiently long to separate the modes in temporal space (by exploiting the fact that each mode propagates with different speed), identification of the mode is not simple. One promising method of doing that is 2D Fourier transform of the sampled signals. In order to do that, signals should be sampled along the axis of the tube both in the temporal and the spatial domains. This generates a 2D array of data (denoted as $g(z,t)$ where z is coordinates along the axis of the tube). A two dimensional Fourier transform of the array both in temporal and spatial space, $G(k_z,\omega)$, decouples the modes in axial wavenumber – frequency space (which will here be referred to as $k-\omega$ space). Since the phase speed of the mode is defined as ω/k_z (recall that k_z can be identified with the real part of the complex wavenumber, q'_{0m}, in the previous section), at given frequency, ω, different phase speeds cause different values of corresponding k_z. Therefore, through the 2D Fourier transform of the sampled signal, $g(z,t)$, each mode can be identified. Once a mode is identified in the $k-\omega$ plot, the attenuation is calculated for the

slice of $k-\omega$ map at given frequency. A spatial inverse Fourier transform performed on this slice (denote $\tilde{g}(z,\omega)$) gives the amplitude change along the axial direction, but with the complication that the modes are mixed. In the case where exponentially decaying oscillating modes are mixed, Prony's method is usually applied to identify the modes with their components of the amplitude and complex wavenumbers. However, Prony's method is sensitively affected by the noise and, sometimes, the results by the Prony's method are ill-posed so that the modified Prony's method is used to minimize such errors (Osborne and Smyth, 1995; Vollmann *et al*, 1997; Dupuis *et al*, 2004). Use of Prony's method for this problem is discussed by Baik *et al.*, (2010). In this report, instead of Prony's method, the complex wavenumbers of the modes are found through the Fast Fourier Transform (FFT). Suppose a mode exists with the form of $g(z) = A\exp(-\delta z)\exp(ik_0 z)$ where A is initial amplitude of the mode, δ is associated damping, and k_0 is real wavenumber of the mode. The symbols, δ and k_z are identical to $\mathrm{Im}[q'_{0m}]$ and $\mathrm{Re}[q'_{0m}]$ respectively in the previous section. Fast Fourier transform for this signal in discrete space can be expressed as:

$$G(k) = \int g(z)e^{-ikz}dz \approx \sum_{n=0}^{N-1} g(n\Delta z)\exp(-ikn\Delta z)\Delta z, \qquad (4.3)$$

where Δz is sampling interval and N is length of the calculation. If length of the sequence of $g(n\Delta z)$ is N_z, then the number of padded zeros is $N - N_z$. Since $g(n\Delta z)$ is zero after the N_z-th element, *m*-th element of $G(k)$ is:

$$G(k_m) \approx A\sum_{n=0}^{N_z-1}\left[\exp(-\delta\Delta z)\exp\{i(k_0 - k_m)\Delta z\}\right]^n \Delta z. \qquad (4.4)$$

Summation of above series can be obtained as follows.

$$G(k_m) \approx A\frac{1-\exp(-N_z\delta\Delta z)\exp\{iN_z(k_0 - k_m)\Delta z\}}{1-\exp(-\delta\Delta z)\exp\{i(k_0 - k_m)\Delta z\}}\Delta z. \qquad (4.5)$$

Therefore, the magnitude of $G(k_m)$ is:

$$|G(k_m)| \approx A\Delta z \sqrt{\frac{1+\exp(-2N_z\delta\Delta z)-2\exp(-N_z\delta\Delta z)\cos\{N_z(k_0-k_m)\Delta z\}}{1+\exp(-2\delta\Delta z)-2\exp(-\delta\Delta z)\cos\{(k_0-k_m)\Delta z\}}}, \quad (4.6)$$

where $k_m = 2\pi(m-1)/(N\Delta z)$. This explains the shape of the spectrum of the oscillating signal which contains attenuation. In the above formulation, the unknown parameters are $A, \delta,$ and k_0. Fitting $G(k_m)$ with the function in Eq. (17), by minimizing the errors estimates for the three unknowns, A, δ, and k_0 minimizing the errors can be obtained. However, those three parameters are not uniquely determined since δ and k_0 also affect the magnitude $G(k_m)$. Therefore, it is necessary to reduce the number of unknown parameters. The real wavenumber, k_0, can be found easily since $|G(k_m)|$ is a maximum when $k_m = k_0$ and Eq. (4.6) becomes:

$$|G(k_0)| \approx A\Delta z \left|\frac{1-\exp(-N_z\delta\Delta z)}{1-\exp(-\delta\Delta z)}\right|. \quad (4.7)$$

Hence, normalizing Eq. (4.6) by Eq. (4.7) (in practical use, this is done by dividing the obtained spectrum in wavenumber space by its maximum magnitude), the normalized magnitude, $|G_n(k_m)|$ becomes:

$$|G_n(k_m)| \approx \left|\frac{1-\exp(-\delta\Delta z)}{1-\exp(-N_z\delta\Delta z)}\right| \sqrt{\frac{1+\exp(-2N_z\delta\Delta z)-2\exp(-N_z\delta\Delta z)\cos\{N_z(k_0-k_m)\Delta z\}}{1+\exp(-2\delta\Delta z)-2\exp(-\delta\Delta z)\cos\{(k_0-k_m)\Delta z\}}}. \quad (4.8)$$

Therefore, Eq. (4.8) contains only one unknown parameter, δ, which is the attenuation of the mode. It can be obtained by fitting the normalized spectrum of the signal in wavenumber space by Eq. (4.8). Figure 4.1 shows Eq. (4.8) as a function of k_m. The number of the sequence, N_z, is chosen as 100 and the sampling interval, Δz, is selected as a 0.01 m step. This corresponds to the actual situation that the signal is sampled along the axis of the tube by 0.01 m step and the total sampling length is 1 m (Baik *et al.*, 2010). The real wavenumber, k_0, is chosen as k_0 = 100 m^{-1} which is close to the wavenumber in the infinite body of pure water at the 23.5 kHz acoustic excitation frequency. Figure 4.1(b) is a magnified picture of Fig. 4.1(a) around the spectral peak. Blue, black, and red curves are calculations for when the

damping, δ, is selected to be 0.5, 1, and 2 m^{-1} respectively. As damping decreases, the subsequent peaks (secondary, tertiary, and so on) become sharper and the dips become more pronounced, and reach lower amplitudes at the minima. As damping increases and the peak of each mode broadens, it eventually merges with its neighbour to the extent that no local minima occur. When the attenuation of the mode is sufficiently high for this to occur, the spectrum has only one spectral peak and other subsequent peaks vanish. Fitting needs to be done with respect to the primary spectral lobe since subsequent lobes have much lower amplitudes and this makes the observation of the changes of the peaks be difficult. Another reason is due to the interference with other spectral components in the case several exponentially decaying modes are mixed in the system. Suppose in Fig. 4.1, (other than the current mode in Fig. 4.1), another mode exist which has spectral peak at 90 m^{-1}. Then, the secondary peaks of the mode whose spectrum is peak at 100 m^{-1} may be buried by the primary lobe of the another mode whose spectrum is peak at 90 m^{-1}. Therefore, fitting should be done with respect to the primary lobe.

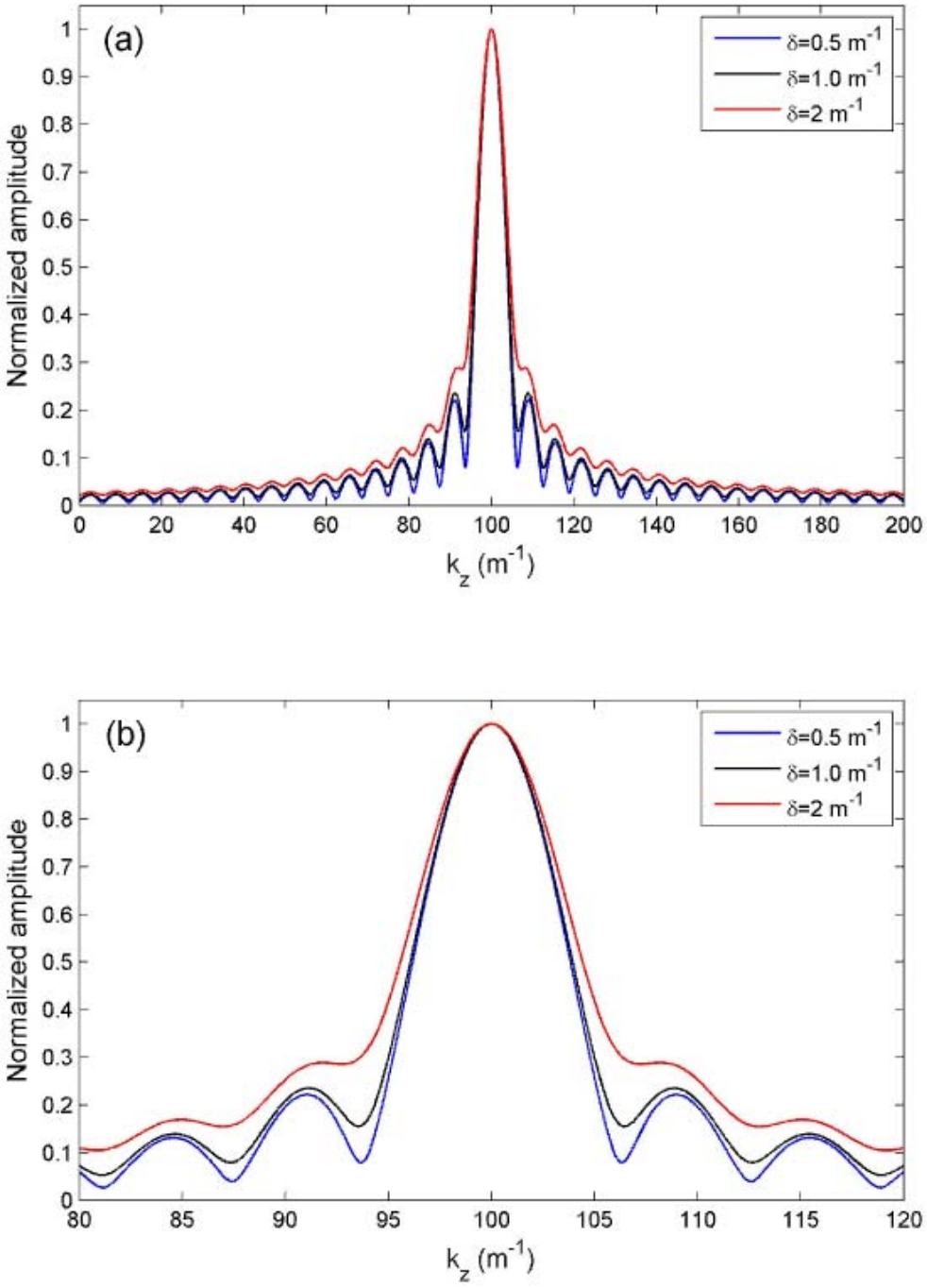

Figure 4.1: Normalized amplitude of the spectrum of the signal by Eq. (4.8) when the damping of the signal is chosen as 0.5 (blue curves), 1.0 (black curves), and 2.0 (red curves) m^{-1} respectively. Parameters of k_0, N_z and Δz are chosen as 100 m^{-1}, 100, and 0.01 m respectively. Panel (b) is the magnified picture of panel (a) around the main spectral peak.

The other option for obtaining the attenuation of the mode is by investigating the amplitude of the spectral peaks by truncating the sampled signal. This is related to the number of the sequence, N_z. The amplitude of the spectral peak is given by Eq. (4.7) which is a function of δ and N_z. Once the signal array is obtained, the controllable variable is N_z. Consider the case in Fig. 4.1. The length of the signal sequence is 100. Figure 4.1 is the spectrum when the Fourier transform is performed on this sequence. If only half of the sequence is considered by truncating the array after 50th measurements or sampling 50 points among 100 measurements, N_z becomes 50 and the resulting spectrum must be different from Fig. 4.1. Thus, when repeating spatial Fourier transform by varying the number of sequence, N_z, the amplitude change of the spectral peak should satisfy Eq. (4.7). In this case, the coefficient, A is also unknown. However, as N_z increases, the resulting amplitude of $|G(k_0)|$ becomes larger since the numerator increases accordingly. Therefore, normalizing Eq. (4.7) by the amplitude of $|G(k_0)|$ when the N_z is chosen as maximum, the result becomes:

$$|G_n(k_0)| \approx \left| \frac{1-\exp(-N_z \delta \Delta z)}{1-\exp(-N_z^{\max} \delta \Delta z)} \right|. \qquad (4.9)$$

Thus, the attenuation also can be obtained through the nonlinear fitting of the change of the amplitude of the spectral peak as a function of the number of the sequence, N_z, by Eq. (4.9). Figure 4.2 shows the normalized amplitude, $|G_n(k_0)|$ described by Eq. (4.9) as a function of N_z. In the extreme case, N_z can be 2, which is the minimum number degree sampling allowable to construct the spectrum (in the actual case, the constructing of the spectrum by sampling two points can be ill-posed). The sampling interval is chosen to be Δz = 0.01 m as in Fig. 4.1. Two different maximum number of the sequence, $N_z^{\max}$, are selected, specifically as 100 in Fig. 4.2(a) and 200 in Fig. 4.2(b). The different colours of the solid curves correspond to the different choices for the damping as indicated in the picture. As damping increases, the curvature of the curve increases. However, when $N_z^{\max} = 100$, although the $\delta = 0.1$ m^{-1} and $\delta = 0.2$ m^{-1} cases are distinct, they are very closely separated. Hence, any fitting performed on the data set which lies along these curves may result in the error of factor 2. However, when the maximum number of sequence, $N_z^{\max} = 200$ in Fig. 4.2(b), the differences between the $\delta = 0.1$ m^{-1} and $\delta = 0.2$ m^{-1} becomes significantly greater than in

the $N_z^{\max} = 100$ case. Consequently the fitting done for this case can enhance the accuracy of the estimated attenuation. Therefore, in order to increase the accuracy with which the attenuation is estimated, it is recommended that the sampling encompasses as much of the signal as the measurement system permits.

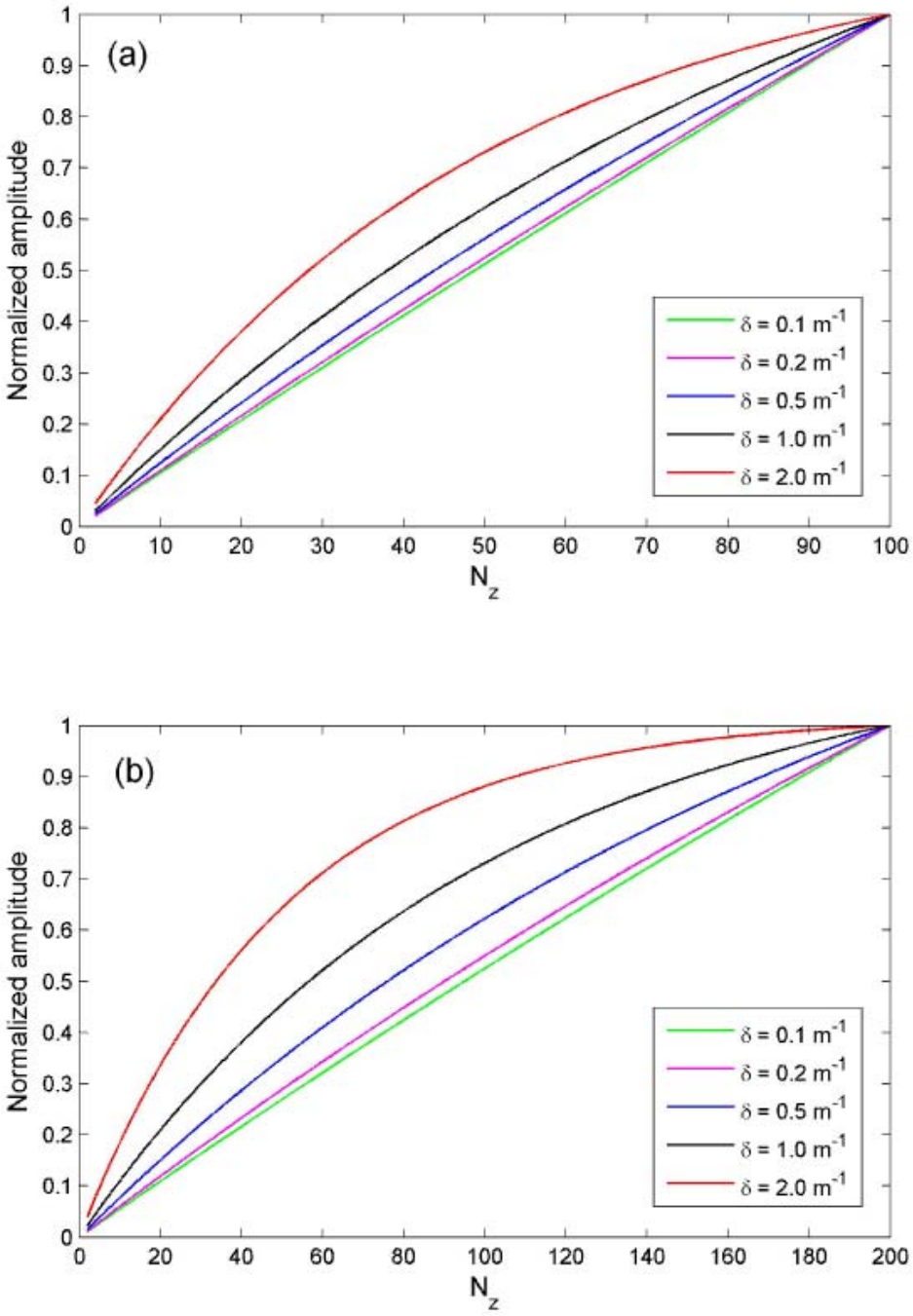

Figure 4.2: Change of the maximum amplitude of the spectrum as a function of the number of sequence, N_z, by Eq. (4.9) when the damping of the signal is chosen as 0.1 (green curves), 0.2 (magenta curves), 0.5 (blue curves), 1.0 (black curves), and 2.0 (red curves) m^{-1} respectively. The sampling interval, Δz, is chosen as 0.01 m. The maximum number of sequence, N_z^{max}, is chosen as (a) 100 and (b) 200 in this calculation.

5 Results

Numerical calculations for the sound speeds and the attenuation are carried out in a water-filled PMMA tube of 4.445 cm inner diameter, and 0.5 cm wall thickness. The published properties of PMMA and water are shown in Table 5.1 (Hartmann and Jarzynski, 1972; Hefner and Marston, 2000). These are the values that are used in the calculations reported in this report, although it is recognized that it is possible that the properties of the real materials may depart from these published values. Because the material properties of plastics can vary even in the same material, direct measurement would be required to ascertain precise and accurate values for the PMMA.

Table 5.1: Elastic property of PMMA and water (Hartmann and Jarzynski, 1972; Hefner and Marston, 2000).

Material	Density (g/cm^3)	Longitudinal velocity (km/s)	Shear velocity (km/s)	Poisson's ratio
PMMA	1.19	2.690	1.340	0.335
Water	1.00	1.479		

Wright *et al*. (1971) measured the elastic constants of the glassy polymers with several samples of the PMMA and the polystyrene. Their measurements showed that the density for PMMA is 1.19 g/cm^3 which is identical to the value in Table 5.1. They also measured longitudinal and shear speeds both in isotropic and anisotropic PMMA at 25 °C. Poisson's ratio can be calculated from the relationship between longitudinal and shear speeds. Isotropic PMMA had 2.689 km/s for the longitudinal velocity and 1.326 km/s for the shear velocity, which returns the corresponding Poisson's ratio as 0.339. For the isotropic PMMA, the elastic properties match the values in Table 5.1 up to the first or the second decimal points. In the case of the anisotropic PMMA, those values were not consistent with the values in the table. One of their samples, which exhibited the greatest variation in the elastic constants, had a range for the longitudinal speed from 2.604 km/s to 3.033 km/s and a range for the shear speed from 1.318 km/s to 1.388 km/s. Hence, the Poisson's ratio varies from 0.328 to 0.368. Thus, it is useful to investigate the sensitivity to change in the numerical calculations due to the variance of the elastic properties within this range. Figure 5.1 shows the modal dispersion curve (lossless solution by Eq. (3.2)) with different choice of the elastic constants both in

ET0 and ET1 modes. The black lines are calculations with our original values in Table 5.1. The blue curves are another calculation, this time obtained from the lowest values of longitudinal and shear speeds of 2.604 km/s and 1.318 km/s respectively in their samples. The red curves are the other calculation obtained from the highest values of longitudinal and shear speeds of 3.033 km/s and 1.388 km/s respectively. The allowed ranges for the variation of the elastic parameters of PMMA shown in Table 5.1 are translated in Fig. 5.1 into variations in the predicted sound speeds for the ET0 and ET1. For the range of frequencies covered by the plot, the two modes show opposite trends in response to this variation in input parameters. As shown in Figure 5.1, when introducing this variance of the elastic constants, the sound speed change in each mode is negligible over most of the range. For the ET1 mode, the phase velocities at the higher frequency range of $kb \geq 3$ for three cases are nearly the same. The ET1 mode shows about 10% variation at the lowest frequencies, the variation reducing at the higher frequencies. The phase velocities for ET1 show very little variation in the plot at frequencies greater than those at the 'knee' for the mode which occurs for ET1 at $kb \sim 3$ (which corresponds to a drive frequency of 16 Hz). In contrast the ET0 mode shows small variation at the lowest frequencies. However the variation in the predicted sound speed tends to increase with increasing frequency as one approaches the highest frequencies shown on the plot (reaching ~5% at $kb \sim 18$, which corresponds to a drive frequency of 95 Hz). Although the differences between the calculated wave speed for the ET0 mode are increasing with increasing frequency at the high-frequency limits of Fig. 5.1, the variance in the phase velocity of ET0 mode is less than 5 percent at these frequencies. This is smaller than the ~10% differences that can be seen at the low frequency range of $kb \leq 3$ for ET1 mode. Therefore, it is sufficient to use the values in Table 5.1 in this frequency range of $kb \leq 18$.

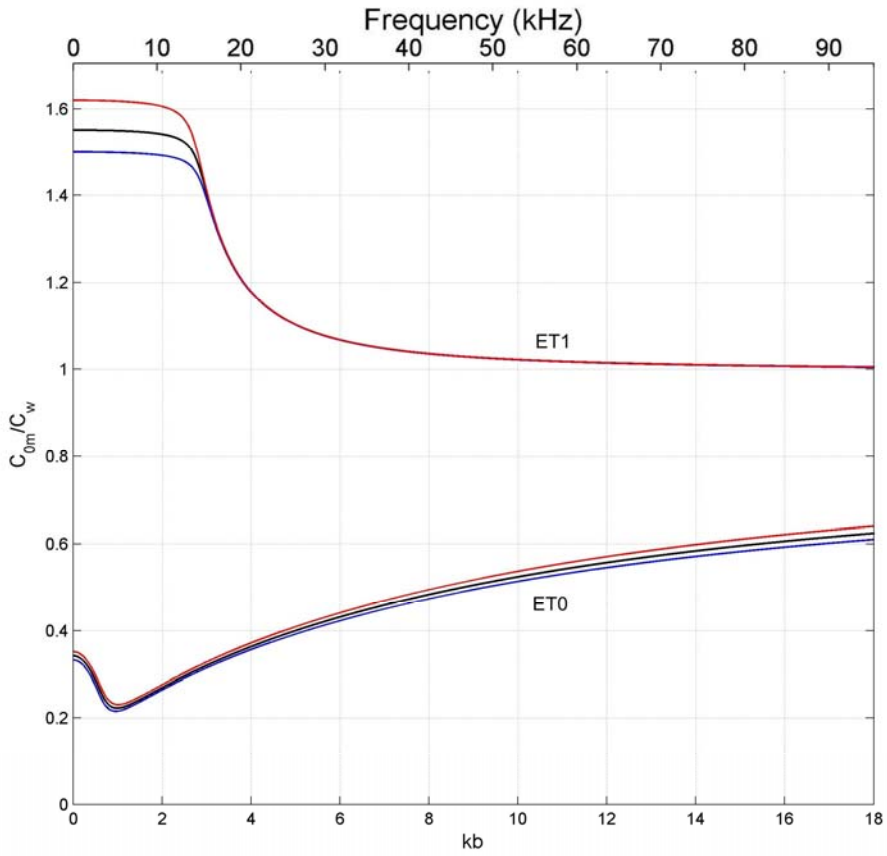

Figure 5.1: Modal dispersion curves with different choice of the elastic constants of PMMA. The black curves are calculation based upon the values listed in Table 5.1. The blue curves are calculation obtained from the values of longitudinal and shear speeds of 2.604 km/s and 1.318 km/s respectively. The red curves are calculation obtained from the values of longitudinal and shear speeds of 3.033 km/s and 1.388 km/s respectively.

The shear viscosity of water is 0.89 cP and the bulk viscosity of water is 3.09 cP (approximately 3 times of the shear viscosity; Litovitz *et al*, 1964). These values are used in the implementation of Eq. (4.1) to obtain the complex solution. Substituting of Eqs. (4.1) and (4.2) into Eq. (3.2) generates the complex solution, the real part of which gives the information on the phase speed and the imaginary part of which is related to the attenuation of the modes. The solid curves in Figure 5.2 show the calculated normalized phase speeds of the modes for the PMMA tube filled with water as a function of dimensionless frequency, $k_1 b$ obtained from the real part of the complex wavenumber, q'_{0m}. The inner radius of the tube is 4.45 cm and the thickness is 0.5 cm. The material property of the PMMA is shown in Table 5. 1. For the comparison with the lossless case, the lossless solutions are superposed as

open circles. This superposition shows that the phase speeds obtained from the complex solutions implemented in this paper are exactly the same as the lossless solutions throughout the frequency range including zero frequency limit and the cut-off frequencies of the ET2 and higher modes.

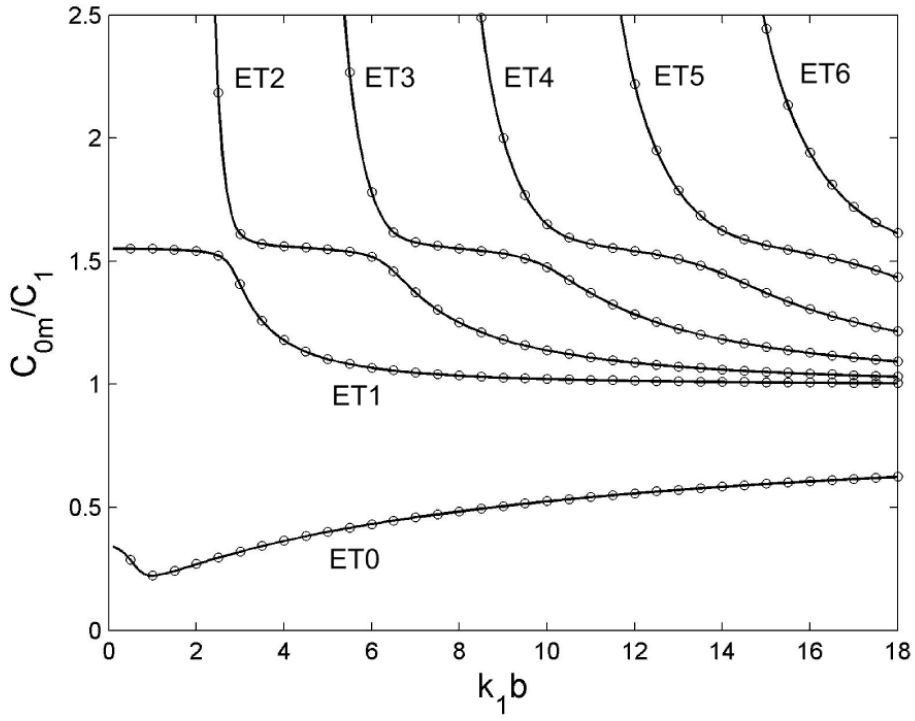

Figure 5.2 Normalized phase velocities of the axisymmetric modes in the water-filled PMMA pipe as a function of normalized frequency. One subsonic mode named ET0 and one supersonic mode named ET1 exist up to zero frequency limit. Open circles are used to indicate lossless solution and solid lines indicate the results of calculations obtained from the real part of the complex solution. The material properties of the PMMA tube are shown in Table 1 (Hartmann and Jarzynski, 1972; Hefner and Marston, 2000).

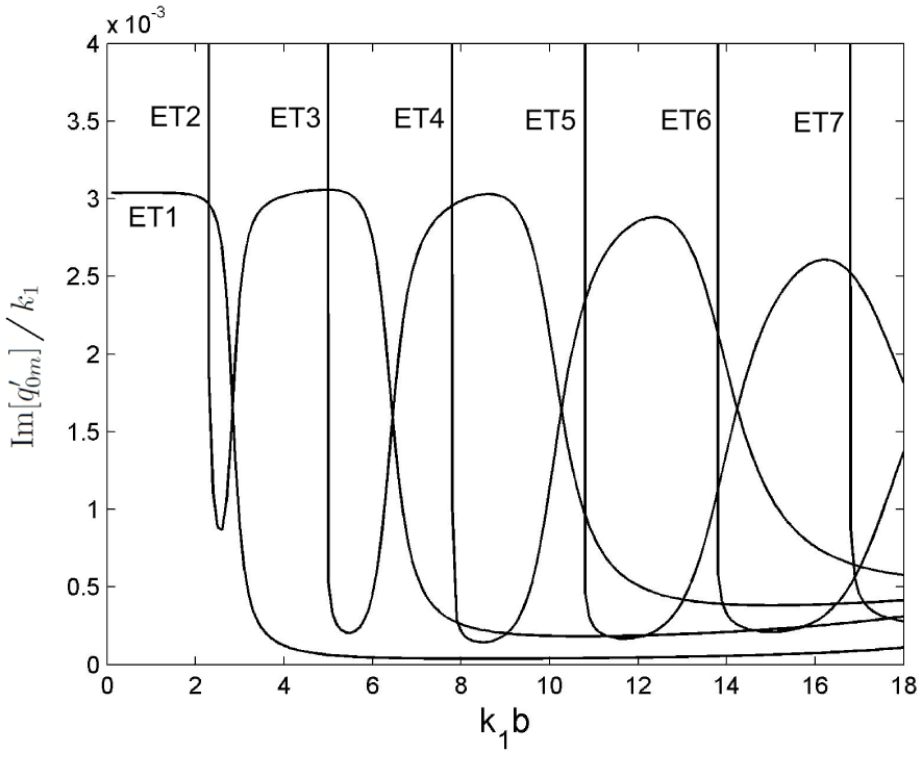

Figure 5.3 Normalized damping of the axisymmetric mode in the water-filled PMMA pipe as a function of normalized frequency. This was obtained from the imaginary part of the complex solution to Eq. (3.2).

While the real part of the complex solution gives the phase speed of the mode, its imaginary part gives the attenuation of the mode as shown in Fig. 5.3. This figure shows the corresponding imaginary part normalized by the wavenumber k_1 as a function of dimensionless frequency. Each mode exhibits a dip in attenuation across a limited frequency range. For example, this trend is observed in $2.3 < k_1 b < 2.9$ for ET2 mode, $4.9 < k_1 b < 6.5$ for ET3 mode, $7.8 < k_1 b < 10.3$ for ET4 mode, and so on. Near the cut-off frequencies of ET2 and the higher modes, their attenuation diverge where corresponding phase speeds become infinite and the group speeds vanish as explained in Fig. 3.3. However, attenuation of the ET1 mode approaches 0.00304 which is the similar order of magnitude as the normalized absorptions defined in Eq. (4.2). The damping of the ET0 mode not plotted in Fig. 5.3 since the damping of the ET0 mode is larger than any other modes over most of the frequency range so that superposing the ET0 damping suppresses the display of the detail structure of the attenuation for other modes. Instead, the ET0 damping is drawn in Fig. 5.4 with the ET1 damping for comparison. From this, the magnitude of the ET0 attenuation is at least three times larger than that of the ET1 mode. It has the maximum attenuation around $k_1 b \approx 0.7$. At

zero frequency limit, the attenuation of the ET0 mode approaches 0.01335 which is about 4 times larger than the attenuation of the ET1 mode.

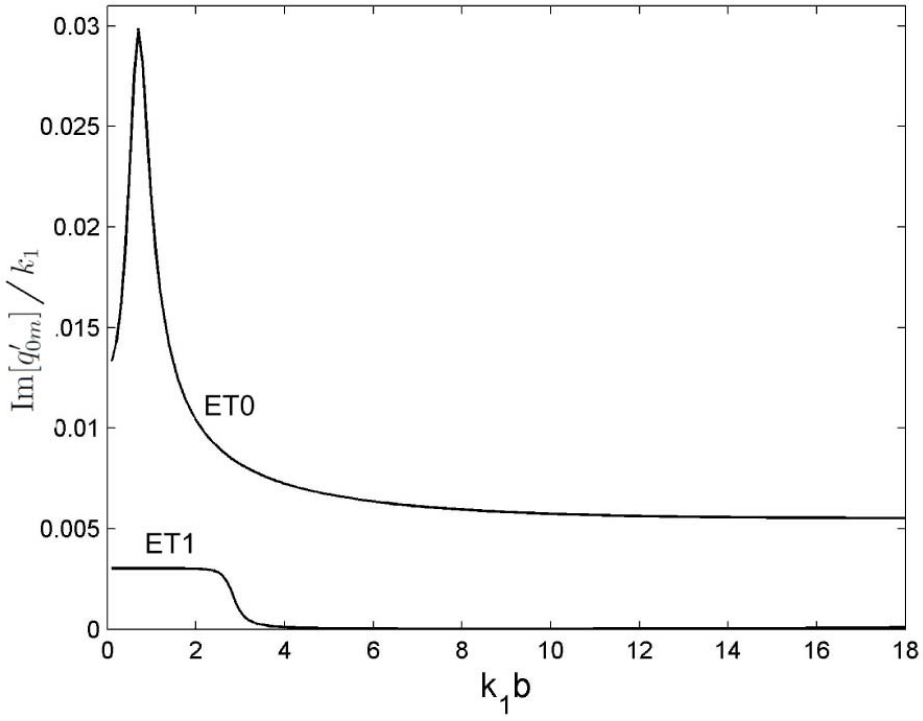

Figure 5.4 Normalized damping of the ET0 mode and the ET1 mode in the water-filled PMMA pipe as a function of normalized frequency. Compared to Fig. 5.3, the damping of the ET0 mode is larger than other modes.

In this way, the complex solutions for the modes inside the PMMA tube filled with water were implemented in this report. This method can be applied to stainless steel pipe filled with liquid mercury that is actually used in the SNS (Spallation Neutron Source) at the ORNL (Oak Ridge National Laboratory) (Baik *et al.*, 2010). Gas bubbles contained in liquid mercury could generate the cavitation damage inside the steel pipe which would cause potential problem of the leakage of toxic and hazardous liquid. To detect such bubbles, the measurements of the phase and group speeds and attenuation are useful. In order to observe the additional attenuation due to the presence of bubbles, the understanding of the attenuation in bubble-free liquid in pipe is important. Hence, the numerical method implemented in this paper can be applied to predict the attenuation along the stainless steel pipe filled with bubble-free liquid mercury.

The actual dimension of the stainless steel pipe in SNS is 6.41 cm for the inner radius and 0.655 cm for the wall thickness. The type of the stainless steel is ss304 and its density is assumed for the purposes of this report to be 7.9 g/cm^3. The longitudinal and shear speeds of the sound in the steel are 5.675 km/s and 3.141 km/s respectively, and the corresponding Poisson's ratio is about 0.28. The ultrasonic absorption of the steel is heavily dependent on the grain size of the metal alloy, frequency, and the temperature. However, in the frequency range used in the calculation in this report, the ultrasonic absorption of the steel is expected to be less than 10^{-4} (Darbari *et al*, 1967). Thus, the corresponding r_c and r_s defined in Eq. (4.2) were set to as zero. The value used for the density of the mercury is 13.5 g/cm^3 which is more than the density of the tube wall. The shear and bulk viscosity coefficients for the mercury are 1.53 cP and 1.90 cP respectively (Jarzynski, 1963). The magnitude of the viscosity coefficients for the mercury are of similar order of magnitude as those for water. However, before finding the complex solutions, the modification of Eq. (4.2) is inevitable in mercury due to the metallic property of the mercury. In most liquids, the absorption by heat conduction is negligible compared to the viscous damping. However, the heat conduction in mercury causes larger attenuation than the viscous damping. This can be easily identified from the Prandtl number that indicates the viscous effect with respect to the thermal conductivity. Hence, the greater the Prandtl number, the more dominant the effect of the liquid viscosity. The Prandtl number of water is 6.75 is high compared to the Prandtl number of mercury, 0.0266 (Kinsler *et al*, 2000). Therefore, in water, the effect of thermal conduction on the damping is at least 1000 times smaller than the viscous effect. In contrast, in mercury, the effect of thermal conduction on the absorption is greater than the viscous effect in mercury. Therefore, in mercury/steel pipe case, the complex wavenumber, k_1', should include the viscous and thermal effects and Eq. (4.2) is modified as follows (Kinsler *et al*, 2000):

$$k_1' \approx k_1 + i\frac{\omega^2}{2\rho_L C_1^3}\left(\frac{4}{3}\eta + \eta_B + \frac{(\gamma-1)\kappa}{c_p}\right), \qquad (5.1)$$

where, for mercury, γ is the ratio of the heat capacities, c_p is the specific heat at constant pressure, and κ is the thermal conductivity. For mercury, the additional term inside the parenthesis, $(\gamma-1)\kappa/c_p$, is calculated as 7.62 cP which is about 4 times larger than the viscous coefficients of the mercury.

As stated in Section 4, when the contribution by the viscosity is minor, using Eq. (3.2) is simpler and it gives the nearly the same numerical precision as using Eq. (2.11). Therefore, in stainless steel tube filled with liquid mercury, substituting the expression of k_1' in Eq. (5.1) and k_s' and k_c' which have $\gamma_s = \gamma_c = 0$ into Eq. (3.2), the complex solutions inside the steel tube filled with liquid mercury can be obtained.

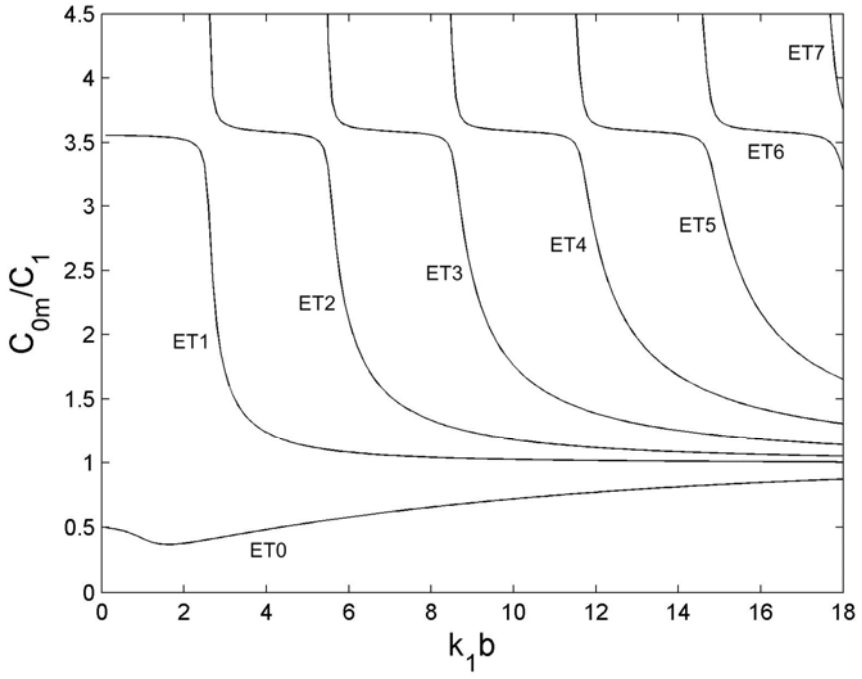

Figure 5.5 Predicted normalized phase velocities of the axisymmetric modes in the mercury-filled steel pipe as a function of normalized frequency.

The phase and group velocities of the modes inside the stainless steel tube filled with liquid mercury are shown in Figure 5.5 as a function of dimensionless frequency. The phase velocities of the modes are normalized by the speed of sound in bulk mercury which is about 1.451 km/s. Comparing these with Figs. 5.2 (or Fig. 3.1) and 3.2 which are the phase and group speeds in PMMA/water tube, many similarities between two cases can be observed. The behaviors of the phase velocity and group velocity at both the zero and high frequency limits are similar. Although the numerical values are different, the frequency dependence of the modes is very similar between two cases. Hence, the acoustical coupling between mercury and the steel (metal) is similar as that between water and the PMMA (plastic). At the

zero frequency limit, the normalized modal phase speeds approach 0.499 for the ET0 mode and 3.577 for the ET1 mode.

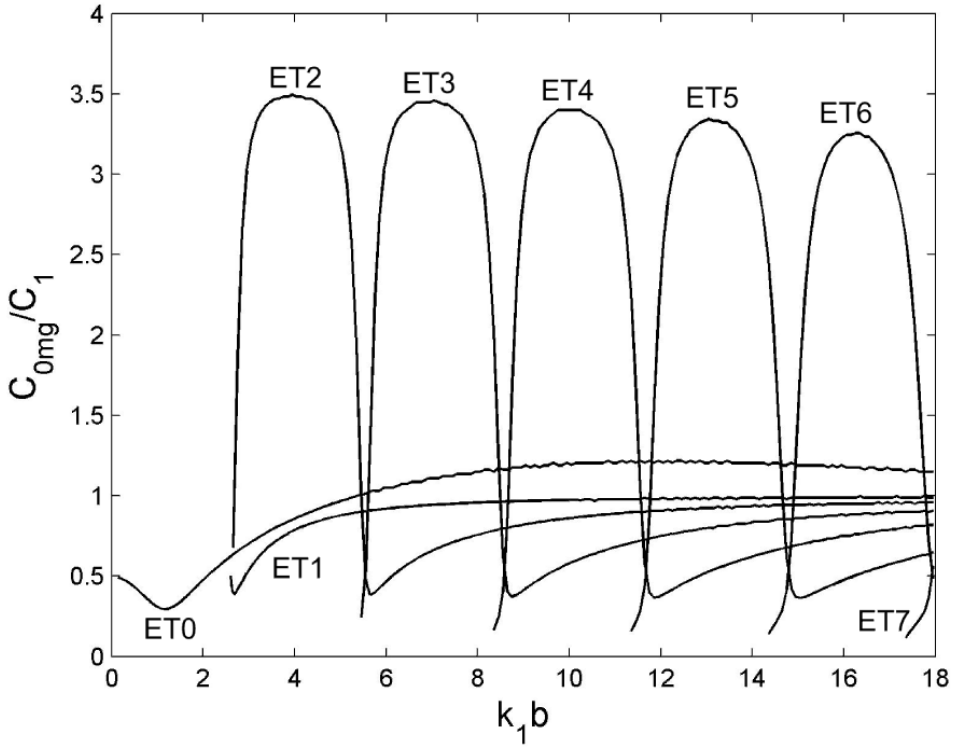

Figure 5.6: Normalized group velocity of axisymmetric modes in the liquid mercury-filled stainless steel pipe as a function of frequency. Compare this with Fig. 3.2.

As with the case in PMMA/water tube, at the cut-off frequencies, the phase speed becomes infinite while the group velocity vanishes. The cut-off frequencies for this mercury/steel pipe can be found from Eq. (3.4) and are listed in Table 5.2.

Table 5.2: Cut-off frequencies of the modes in mercury/steel pipes in dimensionless frequency k_1b.

Mode	ET2	ET3	ET4	ET5	ET6	ET7
k_1b	2.530	5.330	8.249	11.215	14.213	17.235

The predicted attenuation in the steel/mercury pipe obtained from the imaginary part of the complex solution is shown in Fig. 5.7 as a function of a dimensionless frequency. The attenuation is normalized by the real wavenumber in the infinite body of the liquid mercury.

Comparing this with Figs. 5.3 and 5.4, the PMMA/water case, the attenuation of the ET0 mode is less than that of the ET1 at $k_1 b > 2.5$. The attenuation in the mercury/steel system is predicted as at less 1000 times smaller than in the PMMA/water case in the frequency range depicted here. Since the attenuation in bubble-free liquid mercury contained in the steel pipe is so small, the additional damping due to the presence of gas bubbles is predicted to be dominant and easily detected than in PMMA/water case.

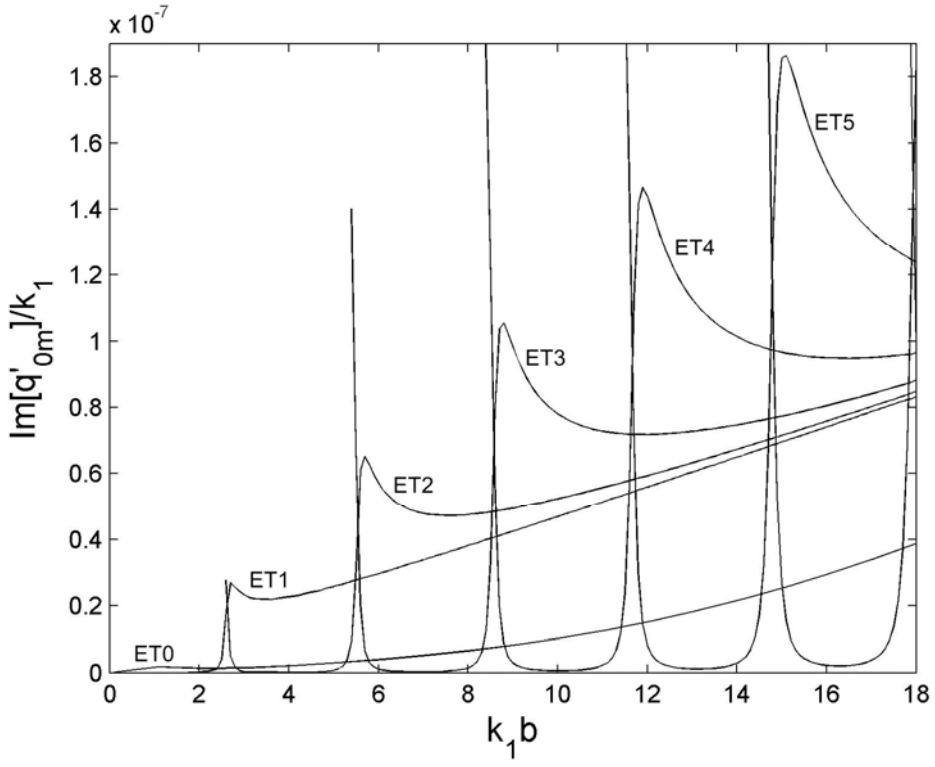

Figure 5.7 Predicted normalized damping of the axisymmetric modes in the mercury-filled steel pipe as a function of normalized frequency. At the frequency range of $k_1 b > 2.5$, the attenuation of the ET0 mode is less than that of the ET1 mode which is opposite to the PMMA/water case. The magnitude of the attenuation is nearly 10^4 times smaller than that observed in the PMMA/water case.

6 Conclusions

Theoretical works by Del Grosso (1971), Lafleur and Shields (1985), and Elvira-Sugura (2000) that describe the propagation of the sound wave inside the elastic tube filled with the bubble-free liquid have been rederived, reviewed and corrected to predict the phase velocity and damping of the modes, and hence to estimate dominant modes and order of magnitudes at a given frequency range in a PMMA tube which is filled with water. In order to obtain the complex solution, complex wavenumbers in liquid and the elastic solids were implemented into the Del Grosso's formulation by introducing the ultrasonic absorption of the liquid and the tube material. The solution was found in complex space and the phase speed was obtained from the real part of the solution which matches with the lossless solution. The damping of the mode was found from the corresponding imaginary part of the complex solution. The method of finding complex wavenumber of the mode in 2D wavenumber-frequency space was theoretically examined which can be implemented in practical case. In a PMMA/water tube with the dimension of the tube described in this report, the attenuation of one subsonic mode, ET0, is predicted to be larger than other modes throughout the frequency. The theory was also applied to the case of mercury-filled steel pipes and the similar features was observed in the phase and group speeds as the PMMA/water case while the attenuation of the modes are much different.

References

Baik K, Jiang J and Leighton T G, “Acoustic attenuation, phase and group velocities in liquid-filled pipes: theory, experiment, and examples of water and mercury”, *Journal of the Acoustical Society of America*, 2010 (submitted).

Darbari GS, Singh RP, and Verma GS, Ultrasonic attenuation in carbon steel and stainless steel at elevated temperatures, *J. Appl. Phys.*, 1968; **39**(5), 2238-2245.

Del Grosso VA, Analysis of multimode acoustic propagation in liquid cylinders with realistic boundary conditions - Application to sound speed and absorption measurements, *Acustica*, 1971; **24**(6), 299-311.

Dupuis P, Sels T, Driesen J, and Belmans R, Exponential parameters measurement using a modified Prony method, *IMTC 2004-IEEE Insrumentation and Measuremen, Technology Conference, Como, Italy*, 2004; 1590-1594.

Elvira-Segura L, Acoustic wave dispersion in a cylindrical elastic tube filled with a viscous liquid," *Ultrasonics* 2000; **37**, 537-547.

Fuller CR and Fahy FJ, Characteristics of wave propagation and energy distributions in cylindrical elastic shells filled with fluid, *J. Sound and Vibrat.* 1982; **81**(4), 501-518.

Grigsby TN and Tajchman EJ, Properties of Lamb waves relevant to the ultrasonic inspection of thin plates, *IRE Trans. Ultra. Eng.* 1961; **UE-8**, 26-33.

Hartmann B and Jarzynski J, Ultrasonic hysteresis absorption in polymers," *J. Appl. Phys.* 1972; **43**(11), 4304-4312.

Hefner BT and Marston PL, Backscattering enhancements associated with subsonic Rayleigh waves on polymer spheres in water: Observation and modelling for acrylic spheres, *J. Acoust. Soc. Am.* 2000; **107**(4), 1930-1936.

Jacobi WJ, Propagation of sound waves along liquid cylinders, *J. Acoust. Soc. Am.* 1948; **21**(2), 120-127.

Jarzynski J, Ultrasonic propagation in liquid Bismuth and Mercury, *Proc. Phys. Soc.* 1963; **81**, 745-750.

Kinsler LE, Frey AR, Coppens AB, and Sanders JV, *Fundamentals of Acoustics*, 2000; 224-234.

Lafleur LD and Shields FD, Low-frequency propagation modes in a liquid-filled elastic tube waveguide, *J. Acoust. Soc. Am.* 1985; **97**(3), 1435-1445.

Lin TC and Morgan GW, Wave propagation through fluid contained in a cylindrical, elastic shell, *J. Acoust. Soc. Am.* 1956; **28**(6), 1165-1176.

Litovitz TA and Davis CM in *Physical Acoustics*, edited by Mason WP, 1964.

Mert B, Sumali H, and Campanella OH, A new method to measure viscosity and intrinsic sound velocity of liquids using impedance tube principles at sonic frequencies, *Rev. Sci. Inst.* 2004; **75**(8), 2613-2619.

Muggleton JM, Brennan MJ, and Pinnington RJ, Wavenumber prediction of waves in buried pipes for water leak detection, *J. Sound and Vibrat.* 2002; **249**(5), 939-954.

Osborne MR and Smyth GK, A modified Prony algorithm for exponential function fitting, *SIAM J. Sci. Comp.* 1995; **16**, 119-138.

Vollmann J, Breu R, and Dual J, High-resolution analysis of the complex wave spectrum in a cylindrical shell containing a viscoelastic medium: Part II. Experimental results versus theory, *J. Acoust. Soc. Am.* 1997; **102**, 909-920.

Wilson PS, Sound propagation and scattering in bubbly liquids. PhD Thesis (Boston University), 2002.

Wilson PS, Reed AH, Wilbur JC, and Roy RA, Evidence of dispersion in an artificial water-saturated sand sediment, *J. Acoust. Soc. Am.* 2007; **121**(2), 824-832.

Wright H, Faraday CSN, White EFT, and Treloar LRG, The elastic constants of oriented glassy polymers", *J. Phys. D: Appl. Phys.* 1971; **4**, 2002-2014.